A Dynamic-Rupture Model of the 2019 M_w 7.1 Ridgecrest Earthquake Being Compatible with the Observations

Zhenguo Zhang[*1,2], Wenqiang Zhang[3], Danhua Xin[1], Kejie Chen[1], and Xiaofei Chen[1]

Abstract

We explore the 2019 M_w 7.1 Ridgecrest earthquake dynamic rupture on the nonplanar fault with homogeneous dynamic parameters using a layered media model. Our model shows that this event produced an average of 1.9 m of right-lateral slip with a maximum slip of ~4.2 m at the place near the epicenter, and the variation of fault-plane strike angles from the middle to the southeastern segment appears to have behaved as a "stress barrier," which postponed the rupture. We also compare the synthetics based on our dynamic rupture with the field records and find good agreement with the static Global Positioning System (GPS) coseismic offsets and strong ground motion waveforms. Our work provides a dynamic-rupture interpretation of the M_w 7.1 Ridgecrest earthquake.

Cite this article as Zhang, Z., W. Zhang, D. Xin, K. Chen, and X. Chen (2020). A Dynamic-Rupture Model of the 2019 M_w 7.1 Ridgecrest Earthquake Being Compatible with the Observations, *Seismol. Res. Lett.* **XX**, 1–7, doi: 10.1785/0220200258.

Supplemental Material

Introduction

On 4 July 2019, an earthquake sequence involving two shocks with magnitudes of M_w 6.4 and M_w 7.1, respectively, occurred near Ridgecrest, California, on an orthogonal fault system (Ross *et al.*, 2019). As the most significant event in southern California over the past decades, the two earthquakes generate intensive interests among public and academic communities. Luckily, only relatively minor damages were caused by the Ridgecrest earthquake sequence. This event was recorded by different instruments, including Interferometric Synthetic Aperture Radar, Global Positioning System (GPS), and strong ground motion network (Hough *et al.*, 2020; Xu *et al.*, 2020). More equipment was deployed to record strong ground motions after this earthquake sequence (Cochran *et al.*, 2020; Hauksson *et al.*, 2020). The dense and high-quality instruments provide us with a valuable opportunity to investigate the earthquakes' rupture and propagation process.

Using regional seismic data, Yang *et al.* (2020) backprojected the ground motion to derive the coseismic rupture for the 2019 Ridgecrest earthquakes. Much work focused on the kinematic rupture of the earthquake sequence by inversion of only geodetic data or joint inversion of geodetic and seismological observations (Barnhart *et al.*, 2019; Liu *et al.*, 2019; Chen *et al.*, 2020; Goldberg *et al.*, 2020; Li *et al.*, 2020). This derived kinematics provided us with insights into the rupture processes of the earthquake. Another view of studying the earthquake source is a dynamic-rupture simulation under the physical assumption (Harris *et al.*, 2018). Lozos and Harris (2020) modeled the M_w 6.4 and M_w 7.1 earthquakes with dynamic-rupture simulations and discussed the foreshock's influences on the mainshock. However, this work needs to be extended to do further dynamic-rupture simulations.

In this work, we investigate the dynamic-rupture process of the 2019 M_w 7.1 Ridgecrest earthquake to consider heterogeneous stress distribution on the fault plane with irregular geometry. The fault geometry is determined by surface-rupture observations and kinematic inversion works. We compare our dynamic simulations with the field observations, including the GPS static displacement and strong-motion velocity waveforms. Our preferred dynamic-rupture model shows good agreement between the observational and synthetic data. Furthermore, we discuss the role of stress orientation on the dynamic rupture. The dynamic-rupture simulations in this work help us better understand the M_w 7.1 Ridgecrest earthquake.

Methods and Parameters

The U.S. Geological Survey reports distinguished surface ruptures related to the mainshock (see red line in Fig. 1), and we follow that to constrain our fault trace. The irregular fault is further divided into three segments: the southeastern, the middle, and the northwestern segments. The earthquake rupture is triggered at the epicenter, which locates between the

1. Department of Earth and Space Sciences, Southern University of Science and Technology, Shenzhen, China; 2. Shenzhen Key Laboratory of Deep Offshore Oil and Gas Exploration Technology, Southern University of Science and Technology, Shenzhen, China; 3. School of Earth and Space Sciences, University of Science and Technology of China, Hefei, China

*Corresponding author: zhangzg@sustech.edu.cn

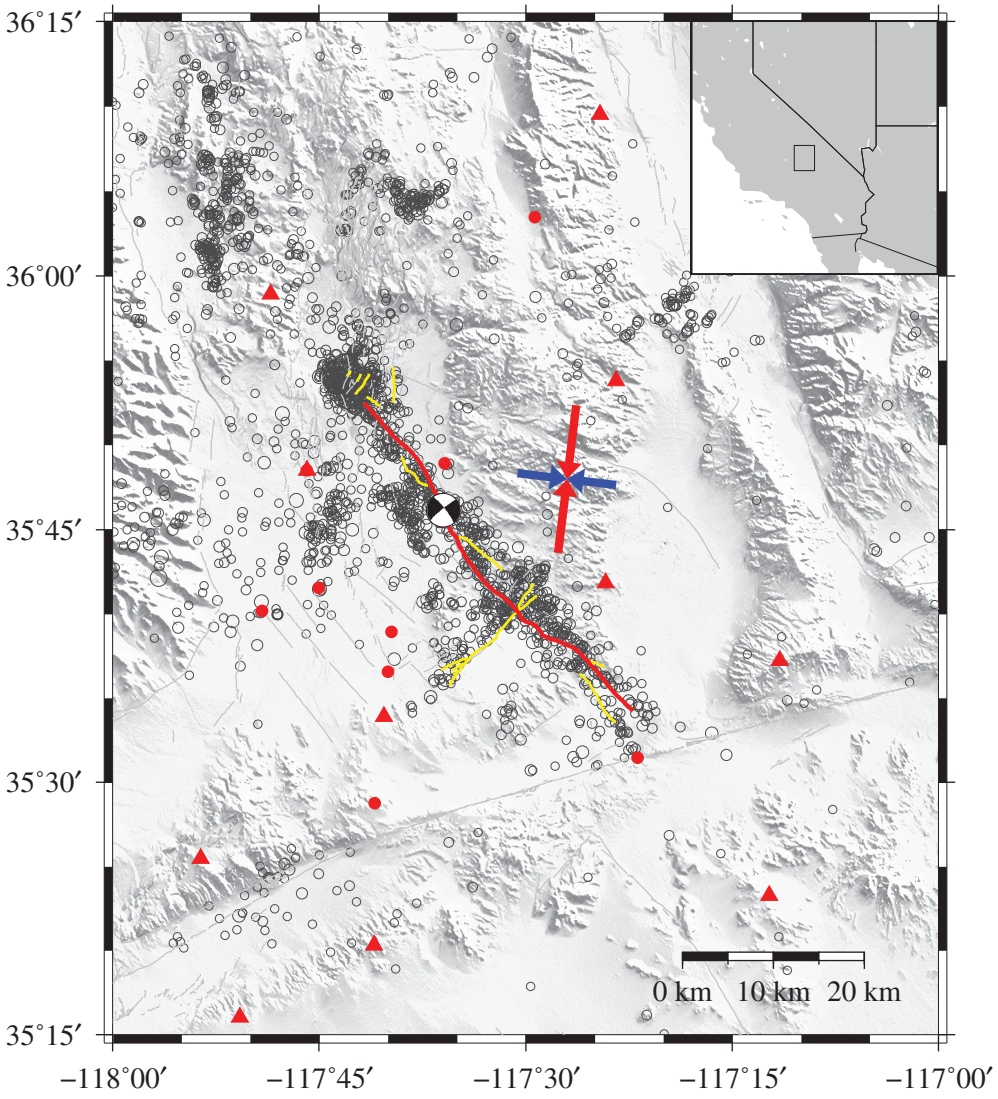

Figure 1. Map view of the 2019 Ridgecrest earthquake. Red and yellow curved lines represent the surface rupture of the M_w 6.4 and M_w 7.1 earthquakes mapped by the U.S. Geological Survey. Light-gray lines are regional faults. Black circles indicate aftershocks with a magnitude larger than 3. Red triangles and solid circles illustrate the Global Positioning System (GPS) and strong ground motion stations used in the static displacement comparisons, respectively. We only model the dynamic rupture and propagation of the M_w 7.1 mainshock, which is highlighted by the red curved line. The black focal mechanism plot represents the mainshock's hypocenter location and source mechanism. The maximum and minimum horizontal stresses are depicted by red and blue arrows, respectively, the lengths and directions of which indicate the relative magnitudes and azimuths of stresses, respectively. The inset map on the top-right shows the location of the study area.

northwestern and middle segments, and then propagates to other segments. We assume that the rupture is fixed within the rupture plane with a width of 15 km (Chen *et al.*, 2020), although some other researchers have assumed different widths (Lozos and Harris, 2020). Moreover, according to the kinematic inversion work (Chen *et al.*, 2020), the dip angle is set as 85°.

The tectonic stress acting on the fault plane is the driving force for triggering an earthquake and keeping its rupture propagating. The more information we know about the background stress field of an earthquake, the better the simulation result we can get by dynamic modeling. The heterogeneous tectonic stress field composed of three principal compressional axes, namely the maximum (S_H) and minimum (S_h) horizontal stresses and the vertical stress (S_v), is used in this work. Inversion works (e.g., Hardebeck and Hauksson, 2001; Yang and Hauksson, 2013) show that the mean azimuth of the maximum horizontal stress in the southern California area is N7°E, although there are some perturbations and errors within the area. Moreover, according to the investigation of the relative magnitude of the three principal stress axes (Hardebeck and Hauksson, 2001), the parameter value of A_ϕ (Simpson, 1997) is set as $A_\phi = 1.5$, which is within the parameter domain of the strike-slip fault. Then, we have $(S_v - S_h)/(S_H - S_h) = 0.5$ according to the definition of Hardebeck and Hauksson (2001). After trial-and-error tests, the maximum horizontal stress S_H value is set as 60 MPa. The values of other principal stresses are listed in Table 1. The other parameters, such as the friction coefficients μ_s and μ_d and the critical slip-weakening distance D_c, are chosen to be within ranges that are widely used in dynamic-rupture simulations (Harris *et al.*, 2018). The following steps are how we set the initial stress conditions on the fault planes. First, the homogeneous stress is resolved onto the nonplanar fault plane. The changing of the strike direction along the fault leads to the heterogeneous distributions of the initial shear and normal stresses in Figure 2. Then, to couple the stress reduction near the free surface, the stress values are linearly tapered to zero at the free surface from the background values at a depth of 5 km. To

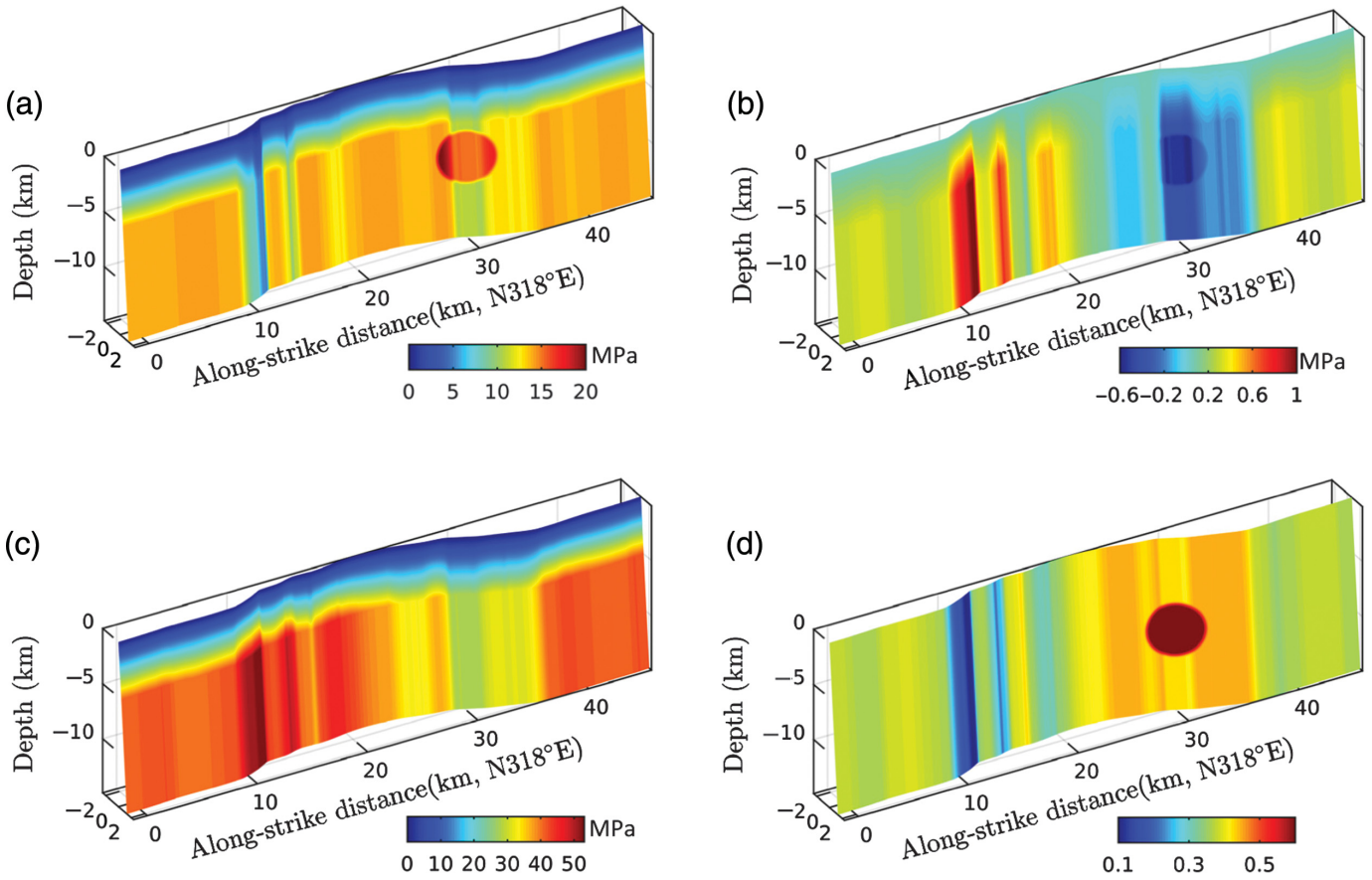

Figure 2. Stress setting on the fault plane of the 2019 Ridgecrest earthquake. Shear stress of (a) strike-slip component with a positive value indicating right-lateral strike-slipping movement, (b) dip-slip component with a positive value indicating reverse-slipping movement, and (c) the normal stress together are resolved on the nonplanar fault by the background stress field illustrated in Figure 1 and listed in Table 1. (d) Distribution of the ratio (μ_0) between the initial stress and the normal stress.

have an initial judgment on the synthetic earthquake's rupture behavior, we show the distribution of μ_0, which is the ratio between shear stress and normal stress, in Figure 2d. The relative relationships of μ_0 to the dynamic and static frictional coefficients (μ_d and μ_s, respectively) reveal the fault's potential rupture ability.

As shown by the initial stress distributions on the fault plane in Figure 2, the connecting part between the southeast and middle segments experiences high normal stress but low shear stress, suggesting that it is hard to host the rupture at this connecting part. By contrast, at the connecting part between the northwest and middle segments, the stress condition is different and favorable to rupture. This may be the reason that the earthquake is nucleated at this segment. The initial stress on the fault plane (Fig. 2) is dominant along the strike direction, indicating that the earthquake is a dominant right-lateral strike-slip type, which is consistent with the kinematic source investigations (Liu *et al.*, 2019).

With the previous parameters defined for the earthquake, we model the dynamic-rupture process with the curved grid finite-difference method (Zhang *et al.*, 2014). The slip-weakening law (Ida, 1972) with the critic slip-weakening distance of 0.3 m is implemented to model the dynamic rupture. Details of the dynamic parameters implemented in this work are listed in Table 1. Moreover, we use a layered media model, which is from Chen *et al.* (2020) and is shown in Table S1 (available in the supplemental material to this article), to depict the media property around the fault plane. The dynamic rupture is triggered at the hypocenter within a circle-shaped nucleation patch with a radius of 2.0 km, in which the initial shear stress is slightly (0.1%) larger than the fault strength, as shown in Figure 2. Then, the rupture is allowed to spontaneously propagate until it is forced to stop by artificial boundaries around the fault except at the free surface. The artificial boundaries are set with high enough strength that cannot be ruptured.

Results

In our dynamic-rupture simulations, the grid interval of 50 m is used to discretize the curved surface along the earthquake plane. The timestep for dynamic simulation is 0.0034 s, with the total running duration of 20 s.

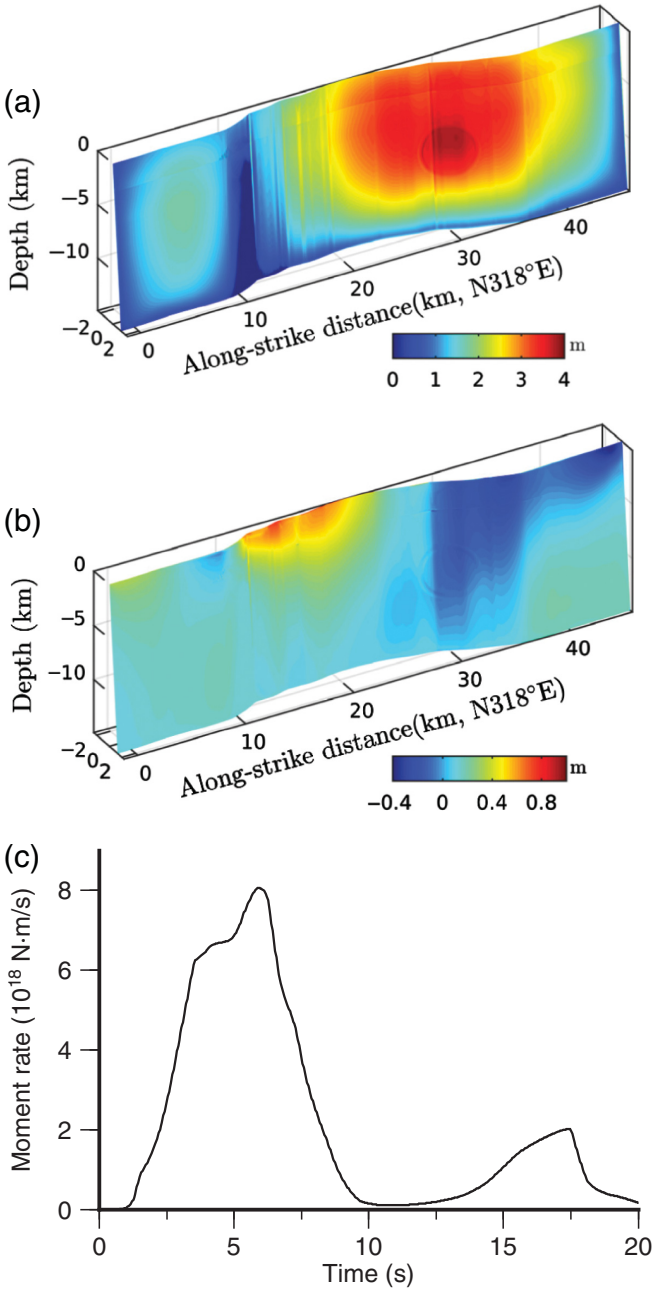

Figure 3. Dynamic simulation results of the Ridgecrest earthquake. (a) Strike-slip and (b) dip-slip distributions on the fault plane. The right-lateral and reverse dislocations for the strike-slip and dip-slip components are indicated by positive values. (c) Moment releasing rate of the dynamic model.

TABLE 1
Parameter Values Used in the Dynamic-Rupture Simulations

Parameter	Value
Modeling parameters	
Element size	50.0 m
Nucleation patch radius	2.0 km
Frictional parameters	
Static friction coefficient, μ_s	0.60
Dynamic coefficient, μ_d	0.25
Critical slip distance, D_c	0.3 m
Principal stress	
Maximum horizontal, S_H	60.0 MPa
Minimum horizontal, S_h	25.0 MPa
Vertical, S_V	42.5 MPa
Azimuth of S_H	N7°E

As shown by our dynamic modeling, the earthquake releases the moment of 4.334×10^{19} N · m, equivalent to M_w 7.09, which is close to the kinematic inversion results. The strike-slip and dip-slip components of the rupture slips are illustrated in Figure 3a,b. The dynamic simulation shows that this event produces an average of 1.9 m right-lateral slip. The largest right-lateral coseismic dislocation occurs near the hypocenter, with a value of ~4.2 m. The moment releasing rate of the dynamic model, as shown in Figure 3c, suggests that the earthquake releases its main energy in the first 10 s of the rupture on the northwest and middle segments. The last pulse comes from the slipping of the southeast segment, which is connected by a part with low initial stress, as shown in Figure 2. There are discrepancies for moment rate functions between our dynamic-rupture modeling as shown in Figure 2 and the kinematic inversions (Liu *et al.*, 2019; Chen *et al.*, 2020). This may be caused by the dynamic model used in this work. Our dynamic simulation shows that the Ridgecrest earthquake ruptures at sub-Rayleigh speed. More detailed information can be found in the video of the rupture process in the supplemental material (Video S1).

Although our forward dynamic-rupture modeling gives time series of ground motion and static displacements at the receivers, it takes too much time, especially when the epicentral distances of the receivers are large. To save time, we choose other methods with more efficiency to calculate the ground motions caused by the dynamic rupture.

We approximate the static displacements with the method proposed by Okada (1992) at stations as illustrated in Figure 1 and compare the synthetic displacements with the observational values in Figure 4. Considering that there are different records that can derive the coseismic static displacements, the observational data recorded at the GPS and ground-motion stations, which are indicated by the triangles and the solid circles, respectively, in Figure 4, are chosen to validate our synthetic displacements. The GPS static displacement data are from UNAVCO Bulletin Board (see Data and Resources), and the coseismic

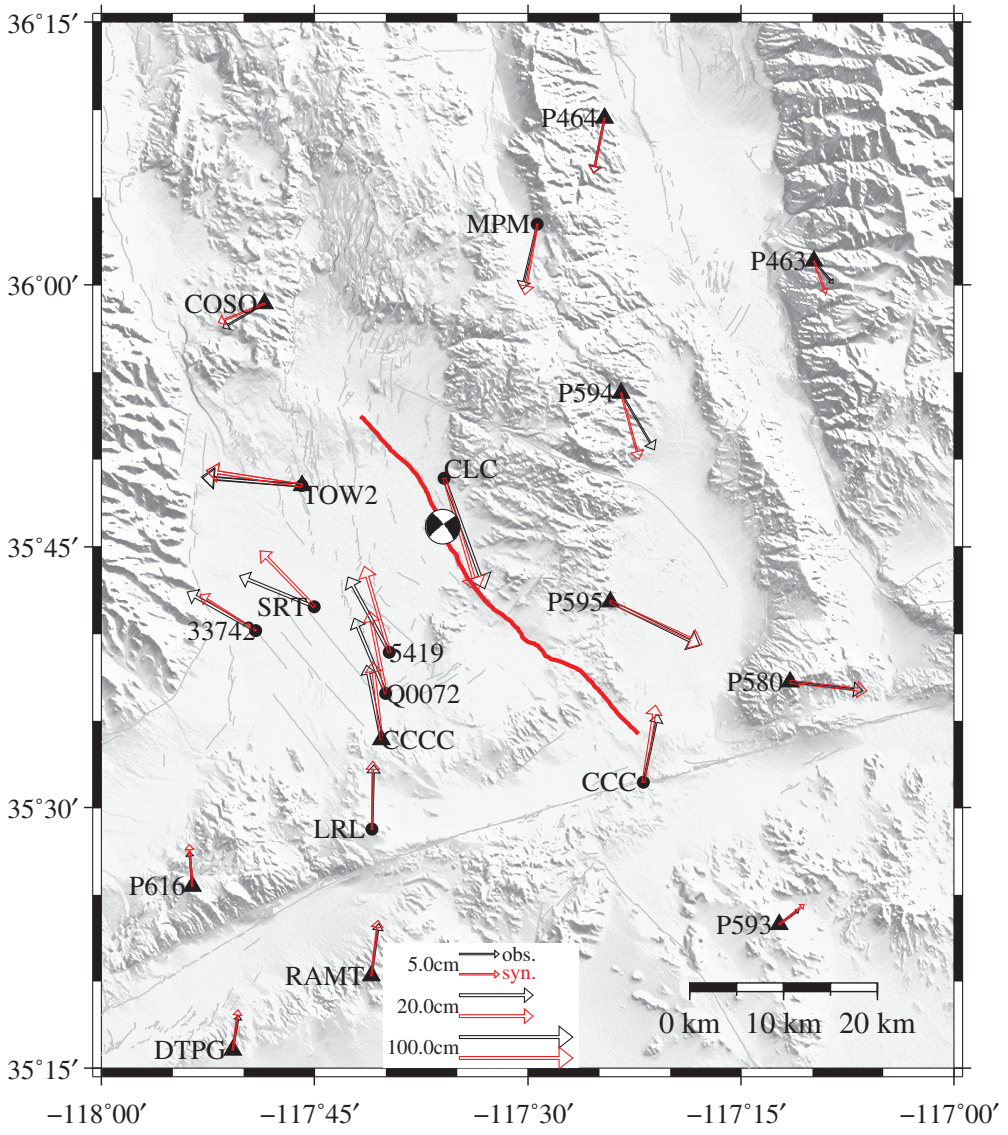

Figure 4. Comparisons of the horizontal static displacements between the observational data (black arrows) and the dynamic rupture simulation results (red arrows). Black triangles and solid circles indicate the GPS and strong ground motion stations, respectively, with the names marked nearby. Note that the absolute values of static displacements are illustrated on a logarithmic scale. The other symbols are the same as in Figure 1.

displacement data at the strong ground motion stations are from Liu *et al.* (2019). We present the observational and synthetic displacements greater than 1.0 cm for the horizontal movements on the logarithmic scale for better visualization. As shown in Figure 4, the observational and synthetic displacements of the M_w 7.1 Ridgecrest earthquake are a good match. Because the M_w 7.1 earthquake is mainly characterized by a right-lateral rupture with slight normal and reverse components according to observations and kinematic source inversions, the vertical parts of the GPS data are small compared with the horizontal components. Moreover, the GPS measurement of the vertical movement has relatively larger uncertainties than those of the horizontal component. Thus, we do not compare the vertical static displacements between the records and synthetic data.

The M_w 7.1 Ridgecrest earthquake was well recorded by waveform instruments during its occurrence. Here, we calculate the particle shaking velocity based on our dynamic-rupture results at selected stations and compare the synthetic seismogram with the instrumental records, as shown in Figure 5. The generalized reflection–transmission matrices (GRTMs) method (Chen, 1990, 1996) is implemented to compute the synthetic seismogram in the layered media as defined in Table S1. The GRTM, an extension of the generalized R/T coefficients method that incorporates the T matrix method, solves the elastodynamic equations in the discrete–wavenumber domain and is suitable for layered media with irregular interfaces due to an arbitrary source (Chen, 1990). The processed data of the M_w 7.1 Ridgecrest earthquake from the Center for Engineering Strong Motion Data (see Data and Resources) are used directly in this work. All of the observational and synthetic data are low-pass filtered with a maximum frequency of 0.2 Hz. The strong ground motion is sensitive to local media under the station and the model we used in the seismogram calculation. The agreements at some stations are not as good as at others. Therefore, in Figure 5, the match between the observational and synthetic seismogram varies across stations. The locations of stations used in Figure 5 are marked in Figure S1. Comparisons at other stations can be found in Figure S2. The waveform comparisons in Figure 5 and Figure S2 between our dynamic forward modeling and the observations show a good match in the main phases, although differences between them still exist in detail. This work focuses on the earthquake source's dynamic rupture with homogeneous parameters, leaving the others relatively simple. Heterogeneities

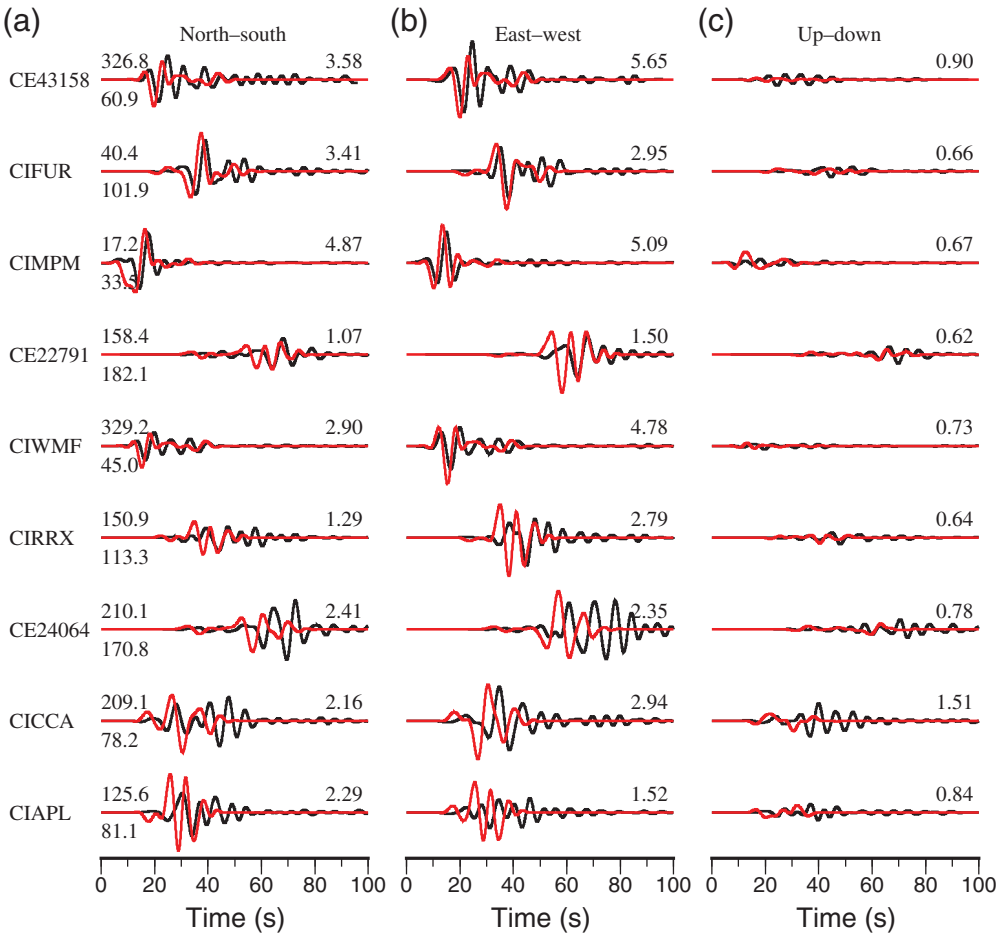

Figure 5. Comparisons of strong ground motions between observations (black) and the dynamic rupture simulations (red). The results of (a) north–south, (b) east–west, and (c) up–down components at selected stations. Station names are marked at the left of the seismogram. Azimuth (degree) and epicentral distance (kilometers) for each station are indicated above and below the north–south-component waveform leader, respectively. The maximum absolute values of each component of the observations (cm/s) are listed at the end of each seismogram.

given by inversions in dynamic rupture and the media properties may improve the agreements between the synthetic and observational ground motions.

Discussion and Conclusion

In this work, we modeled the dynamic-rupture process of the 2019 M_w 7.1 Ridgecrest earthquake and compared our simulation results with observational data recorded at GPS and ground-motion stations. The homogeneous background stress described by three compressional principal stresses and their azimuths was resolved on the nonplanar fault geometry. The comparison between the dynamic rupture model and observations revealed a good match between observational results and modeled results in general, despite some misfits for the strong ground motion data.

Various sources of uncertainties from the media model, fault geometry, stress status, and friction properties of rock could significantly affect the dynamic simulation performance. We did not implement the inversion strategy involving minimizing the misfit between observations and dynamic modeling to get an optimal dynamic model. The dynamic inversion expects more reliable dynamic parameters of the earthquake (Ruiz and Madariaga, 2011; Herrera *et al.*, 2017; Gallovič *et al.*, 2019), but this is beyond the topic of this work and can be investigated by future works.

Data and Resources

The aftershock catalog is obtained from https://scedc.caltech.edu/research-tools/QTM-ridgecrest.html, and the surface rupture data are from the U.S. Geological Survey (https://www.usgs.gov/media/images/surface-ruptures-july-4-and-5-ridgecrest-ca-earthquakes). The Global Positioning System (GPS) coseismic displacement data are obtained from the UNAVCO Bulletin Board (https://www.unavco.org/highlights/2019/ridgecrest.html). The strong ground motion data are downloaded from the Center for Engineering Strong Motion Data (https://www.strongmotioncenter.org/index.html). All websites were last accessed in November 2020. The supplemental material for this article includes a table of the layer media model that we implemented in the dynamic-rupture simulation and seismogram calculations, a figure showing the stations used for seismogram comparison, a figure showing the comparison between the dynamic modeling and observations at other stations, and a video showing the snapshots of the dynamic-rupture process of the earthquake.

Acknowledgments

The authors are grateful to Editor Allison Bent as well as two anonymous reviewers for their constructive comments. This work is supported by the National Natural Science Foundation of China (Grants 41922024 and 41790465) and Shenzhen Key Laboratory of Deep Offshore Oil and Gas Exploration Technology (Grant Number ZDSYS20190902093007855). This work is supported by the Center for Computational Science and Engineering at Southern University of Science and Technology.

References

Barnhart, W. D., G. P. Hayes, and R. D. Gold (2019). The July 2019 Ridgecrest, California, earthquake sequence: Kinematics of slip and stressing in cross-fault ruptures, *Geophys. Res. Lett.* **46,** no. 21, 11,859–11,867, doi: 10.1029/2019GL084741.

Chen, K., J.-P. Avouac, S. Aati, C. Milliner, F. Zheng, and C. Shi (2020). Cascading and pulse-like ruptures during the 2019 Ridgecrest earthquakes in the eastern California shear zone, *Nat. Commun.* **11,** no. 1, 1–8, doi: 10.1038/s41467-019-13750-w.

Chen, X. (1990). Seismogram synthesis for multi-layered media with irregular interfaces by global generalized reflection/transmission matrices method. I. Theory of two-dimensional *SH*case, *Bull. Seismol. Soc. Am.* **80,** no. 6, 1696–1724.

Chen, X. (1996). Seismogram synthesis for multi-layered media with irregular interfaces by global generalized reflection/transmission matrices method. III. Theory of 2D *P-SV* case, *Bull. Seismol. Soc. Am.* **86,** no. 2, 389–405.

Cochran, E. S., E. Wolin, D. E. McNamara, A. Yong, D. Wilson, M. Alvarez, N. van der Elst, A. McClain, and J. Steidl (2020). The U.S. Geological Survey's rapid seismic array deployment for the 2019 Ridgecrest earthquake sequence, *Seismol. Res. Lett.* **91,** no. 4, 1952–1960, doi: 10.1785/0220190296.

Gallovič, F., L. Valentová, J.-P. Ampuero, and A.-A. Gabriel (2019). Bayesian dynamic finite-fault inversion: 2. Application to the 2016 M_w 6.2 Amatrice, Italy, earthquake, *J. Geophys. Res.* **124,** 6970–6988, doi: 10.1029/2019JB017512.

Goldberg, D. E., D. Melgar, V. J. Sahakian, A. M. Thomas, X. Xu, B. W. Crowell, and J. Geng (2020). Complex rupture of an immature fault zone: A simultaneous kinematic model of the 2019 Ridgecrest, CA earthquakes, *Geophys. Res. Lett.* **47,** no. 3, e2019GL086382, doi: 10.1029/2019GL086382.

Hardebeck, J. L., and E. Hauksson (2001). Crustal stress field in southern California and its implications for fault mechanics, *J. Geophys. Res.* **106,** no. B10, 21,859–21,882, doi: 10.1029/2001JB000292.

Harris, R. A., M. Barall, B. Aagaard, S. Ma, D. Roten, K. Olsen, B. Duan, D. Liu, B. Luo, K. Bai, *et al.* (2018). A suite of exercises for verifying dynamic earthquake rupture codes, *Seismol. Res. Lett.* **89,** no. 3, 1146–1162, doi: 10.1785/0220170222.

Hauksson, E., C. Yoon, E. Yu, J. R. Andrews, M. Alvarez, R. Bhadha, and V. Thomas (2020). Caltech/USGS Southern California Seismic Network (SCSN) and Southern California Earthquake Data Center (SCEDC): Data availability for the 2019 Ridgecrest sequence, *Seismol. Res. Lett.* **91,** no. 4, 1961–1970, doi: 10.1785/0220190290.

Herrera, C., S. Ruiz, R. Madariaga, and P. Poli (2017). Dynamic inversion of the 2015 Jujuy earthquake and similarity with other intraslab events, *Geophys. J. Int.* **209,** no. 2, 866–875, doi: 10.1093/gji/ggx056.

Hough, S. E., E. Thompson, G. A. Parker, R. W. Graves, K. W. Hudnut, J. Patton, T. Dawson, T. Ladinsky, M. Oskin, K. Sirorattanakul, *et al.* (2020). Near-field ground motions from the July 2019 Ridgecrest, California, earthquake sequence, *Seismol. Res. Lett.* **91,** no. 3, 1542–1555, doi: 10.1785/0220190279.

Ida, Y. (1972). Cohesive force across the tip of a longitudinal-shear crack and Griffith's specific surface energy, *J. Geophys. Res.* **77,** no. 20, 3796–3805.

Li, S., G. Chen, T. Tao, P. He, K. Ding, R. Zou, J. Li, and Q. Wang (2020). The 2019 M_w 6.4 and M_w 7.1 Ridgecrest earthquake sequence in eastern California: Rupture on a conjugate fault structure revealed by GPS and InSAR measurements, *Geophys. J. Int.* **221,** no. 3, 1651–1666, doi: 10.1093/gji/ggaa099.

Liu, C., T. Lay, E. E. Brodsky, K. Dascher-Cousineau, and X. Xiong (2019). Coseismic rupture process of the large 2019 Ridgecrest earthquakes from joint inversion of geodetic and seismological observations, *Geophys. Res. Lett.* **46,** no. 21, 11,820–11,829, doi: 10.1029/2019GL084949.

Lozos, J., and R. Harris (2020). Dynamic rupture simulations of the M6.4 and M7.1 July, 2019 Ridgecrest, California earthquakes, *Geophys. Res. Lett.* **47,** no. 7, e2019GL086020, doi: 10.1029/2019GL086020.

Okada, Y. (1992). Internal deformation due to shear and tensile faults in a half-space, *Bull. Seismol. Soc. Am.* **82,** no. 2, 1018–1040.

Ross, Z. E., B. Idini, Z. Jia, O. L. Stephenson, M. Zhong, X. Wang, Z. Zhan, M. Simons, E. J. Fielding, S.-H. Yun, *et al.* (2019). Hierarchical interlocked orthogonal faulting in the 2019 Ridgecrest earthquake sequence, *Science* **366,** no. 6463, 346–351, doi: 10.1126/science.aaz0109.

Ruiz, S., and R. Madariaga (2011). Determination of the friction law parameters of the M_w 6.7 Michilla earthquake in northern Chile by dynamic inversion, *Geophys. Res. Lett.* **38,** L09317, doi: 10.1029/2011GL047147.

Simpson, R. W. (1997). Quantifying Anderson's fault types, *J. Geophys. Res.* **102,** no. B8, 17,909–17,919, doi: 10.1029/97JB01274.

Xu, X., D. T. Sandwell, and B. Smith-Konter (2020). Coseismic displacements and surface fractures from Sentinel-1 InSAR: 2019 Ridgecrest earthquakes, *Seismol. Res. Lett.* **91,** no. 4, 1979–1985, doi: 10.1785/0220190275.

Yang, J., H. Zhu, and D. Lumley (2020). Time-lapse imaging of coseismic ruptures for the 2019 Ridgecrest earthquakes using multi-azimuth back-projection with regional seismic data and a 3D crustal velocity model, *Geophys. Res. Lett.* **47,** no. 9, e2020GL087181, doi: 10.1029/2020GL087181.

Yang, W., and E. Hauksson (2013). The tectonic crustal stress field and style of faulting along the Pacific North America plate boundary in southern California, *Geophys. J. Int.* **194,** no. 1, 100–117.

Zhang, Z., W. Zhang, and X. Chen (2014). Three-dimensional curved grid finite-difference modelling for non-planar rupture dynamics, *Geophys. J. Int.* **199,** no. 2, 860–879, doi: 10.1093/gji/ggu308.

Manuscript received 27 July 2020
Published online 16 December 2020